Supporting Information for "Lithospheric sill intrusions and present-day ground deformation at Rhenish Massif, Central Europe"

F. Silverii[1,2], L. Mantiloni[1,3], E. Rivalta[1,4], T. Dahm[1,3]

[1]Physics of Earthquakes and Volcanoes, German Research Centre for Geosciences (GFZ), Potsdam, Germany

[2]National Institute for Geophysics and Volcanology (INGV), Osservatorio Nazionale Terremoti, Rome, Italy

[3]Institute of Geosciences, University of Potsdam, Potsdam, Germany

[4]Department of Geophysics, University of Bologna, Bologna, Italy

Contents of this file

Introduction

This supporting information includes further details about the inversion methods and gravity change estimation introduced in the main text, and complementary figures for the data and results description.

Text S1. Methods of regularization parameter selection and model parameters uncertainty estimation

Once the forward problem is defined as in equation (2) of the main text, different methods exist to select the optimal value for the regularization parameter k. The L-curve method consists in picking k from the knee of a trade-off curve between model-roughness ($\sqrt{(\mathbf{Lm})^T\mathbf{Lm}}/M$) and data-misfit (in terms of – unitless – weighted residual sum of squares WRSS = $\mathbf{(d\text{-}Gm)}^T\mathbf{W}^T\mathbf{W(d\text{-}Gm)}$) produced by solving the inversion with different values of k. This method is intuitive and fast to implement, but the selection retains a level of subjectivity if the knee curve point is not well defined. The cross-validation (CV) method is based on the idea that the model parameters recovered by the inversion of a subsample of the dataset (the training set) should be able to predict the data that were not used in the inversion (the validation set). The original data set is randomly partitioned into n subsamples, a single subsample is considered as the validation set, and the remaining $n-1$ subsamples are used as the training set. This test is performed for different values of the smoothing parameter, that are then compared in terms of the CVSS (cross-validation sum of squares of the predicted residuals), representing a measure of the model ability to predict observation. The most appropriate smoothing parameter is the one resulting in the lowest CVSS.

Testing both methods, we found that L-curve and CV give compatible results for the GPS-sites case, with CV providing a clearer minimum (Figure S4a). For the gridded-data cases, instead, the L-curve produces a better-defined knee, whereas the CV solutions tend to be slightly under-smoothed, particularly for the gridded-std2 case (Figure S4b, S4c). We therefore selected smoothing factors through CV for the GPS-data case and through

L-curve for the gridded-data cases.

We have applied the bootstrap statistical method (Efron & Tibshirani, 1986) with 1500 runs in order to estimate opening rates uncertainties. This technique consists in creating synthetic datasets by randomly selecting, with replacement, N points from the original dataset, where N is the number of GPS sites/grid points. For the new sample of N points (some of which are redundant selections from the original sample, while some points in the original sample are missing), the opening-rate distribution is recomputed using the same inversion method explained in Section 3 of the main text. By implementing this process many times, a distribution of opening rates values is constructed for each patch and, from this, a meaningful statistical uncertainty value can be estimated.

Text S2. Gravity change estimation

We estimated the total expected gravity changes at the free surface of an elastic half-space associated to our TRDs model (assuming 30 km depth) using the solutions from Okubo (1992) as implemented by Beauducel (2022). The expected gravity signal is dominated by the free-air effect so that its spatial pattern is similar to the modeled uplift. Assuming a half-space density of 2600 kg/m^3 and a lower density for the intruding material, we obtain a total gravity change up to about -0.3 μGal/yr. This corresponds to 0.1 μGal/yr after removal of the free-air contribution estimated using the predicted uplift and the theoretical free-air gradient -308.6 μGal/m.

References

Beauducel, F. (2022). OKUBO: Gravity change due to shear and tensile faults [Software]. *MATLAB Central File Exchange*. Retrieved from https://www.mathworks.com/matlabcentral/fileexchange/37158-okubo-gravity-change-due-to-shear-and-tensile-faults

Efron, B., & Tibshirani, R. (1986). Bootstrap Methods for Standard Errors, Confidence Intervals, and Other Measures of Statistical Accuracy. *Statistical Science*, *1*(1), 54 – 75. doi: 10.1214/ss/1177013815

Kreemer, C., Blewitt, G., & Davis, P. M. (2020). Geodetic evidence for a buoyant mantle plume beneath the Eifel volcanic area, NW Europe [Dataset]. *Geophysical Journal International*, *222*(2), 1316-1332. doi: 10.1093/gji/ggaa227

Okubo, S. (1992). Gravity and potential changes due to shear and tensile faults in a half-space. *Journal of Geophysical Research: Solid Earth*, *97*(B5), 7137-7144. doi: 10.1029/92JB00178

Wessel, P., Smith, W. H., Scharroo, R., Luis, J., & Wobbe, F. (2013). Generic mapping tools: improved version released. *Eos, Transactions American Geophysical Union*, *94*(45), 409–410. doi: https://doi.org/10.1002/2013EO450001

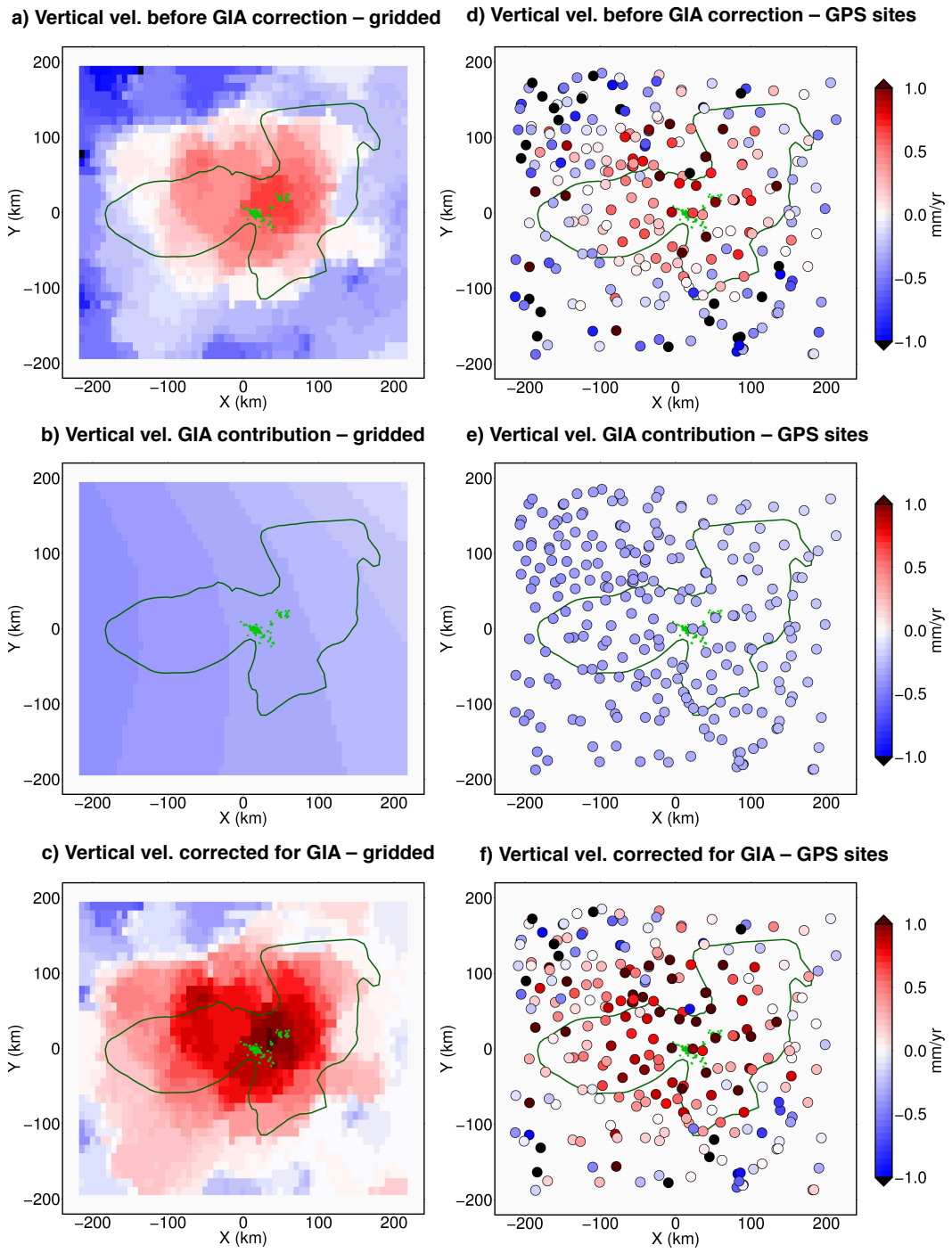

Figure S1. Vertical velocities correction for the GIA contribution. Data in a), c) and d) are provided by Kreemer et al. (2020); b) represents the GIA contribution as estimated from the difference between a) and c). This contribution has been then interpolated at the GPS sites locations (e) and used to correct the vertical velocities at GPS sites in d). The final result is showed in f). Green dots are centers of Quaternary EVF activity, and dark green outline is Rhenish Massif.

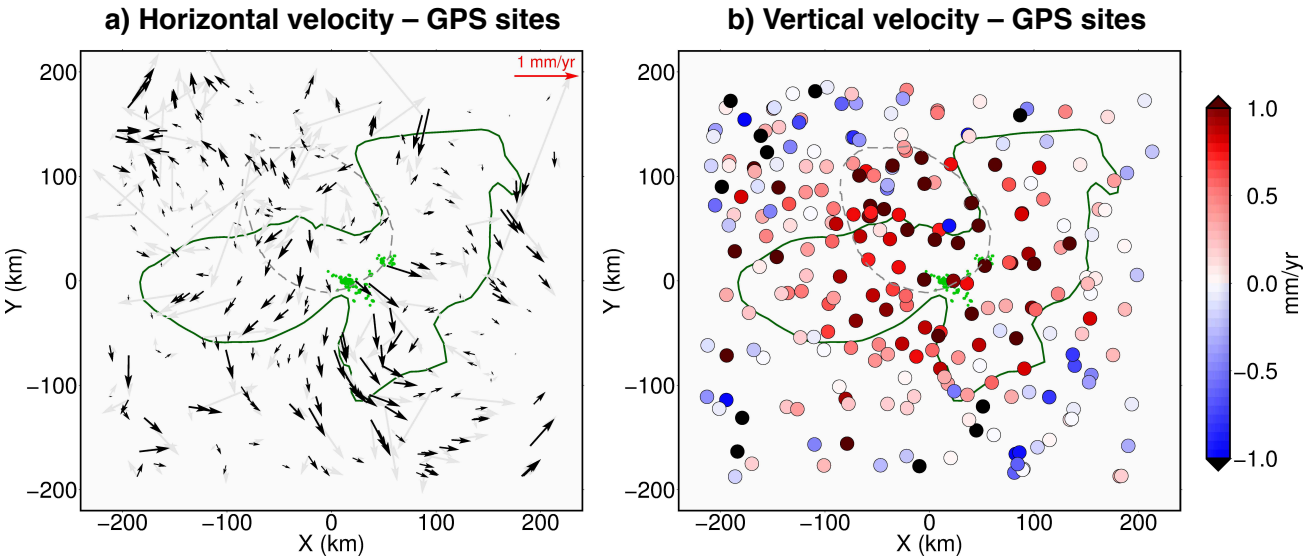

Figure S2. Same as Figure 1c, 1d in the main text, but filtered horizontal velocities (black arrows) are shown together with the original ones (grey arrows) in order to highlight and show more clearly the underlying horizontal deformation. The filtering consists in first applying a block average by L1 norm and then continuous curvature splines over 30 km spacing grid (using respectively *blockmedian* and *surface* algorithms by Generic Mapping Tool; Wessel et al., 2013). All other elements are the same as Figure S1.

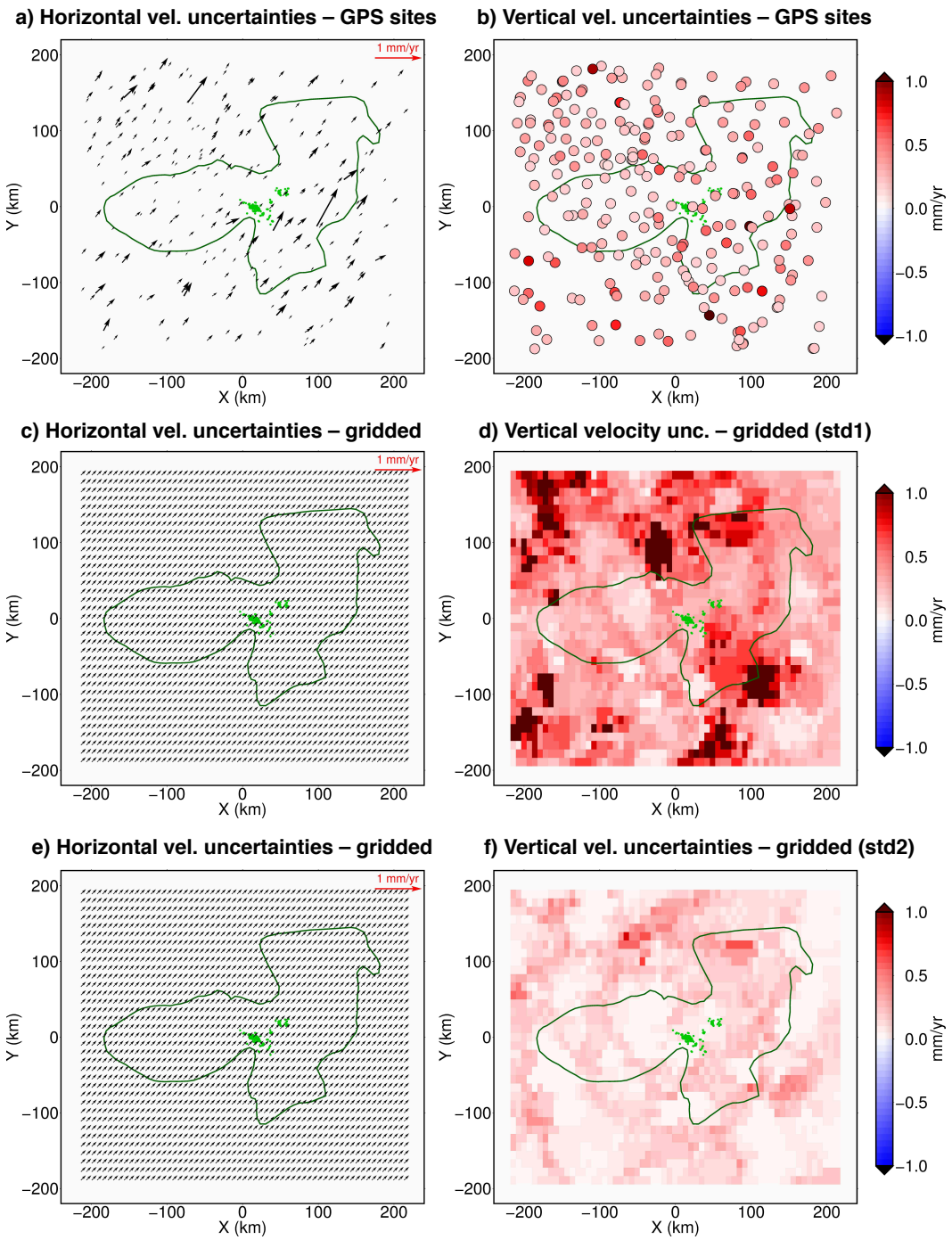

Figure S3. Spatial distribution of velocity uncertainties at GPS sites (a, b) and gridded values (c to f). The latter are shown in two different ways for vertical uncertainty: respectively difference from raw GPS values (c, d) and from despeckled GPS values (e, f) (See Kreemer et al. (2020) for further details about uncertainty computation). All other elements are the same as Figure S1.

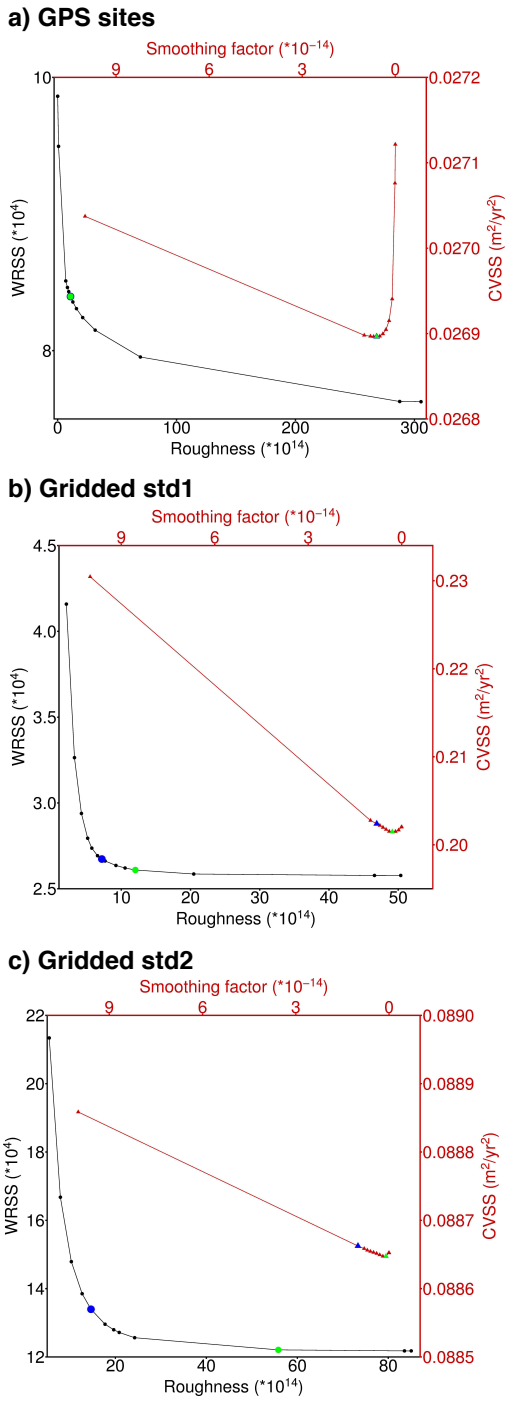

Figure S4. Plots of L-curves (black line) and CV curves (red lines) associated with the solutions for a TRDs grid at 30 km depth. The blue symbols indicate the selected smoothing factor values from L-curve (corresponding to the solutions in Figure 2 of the main text). The green symbols indicate the smoothing factor as selected from CV. Note that the blue and green symbols coincide for the GPS data case.

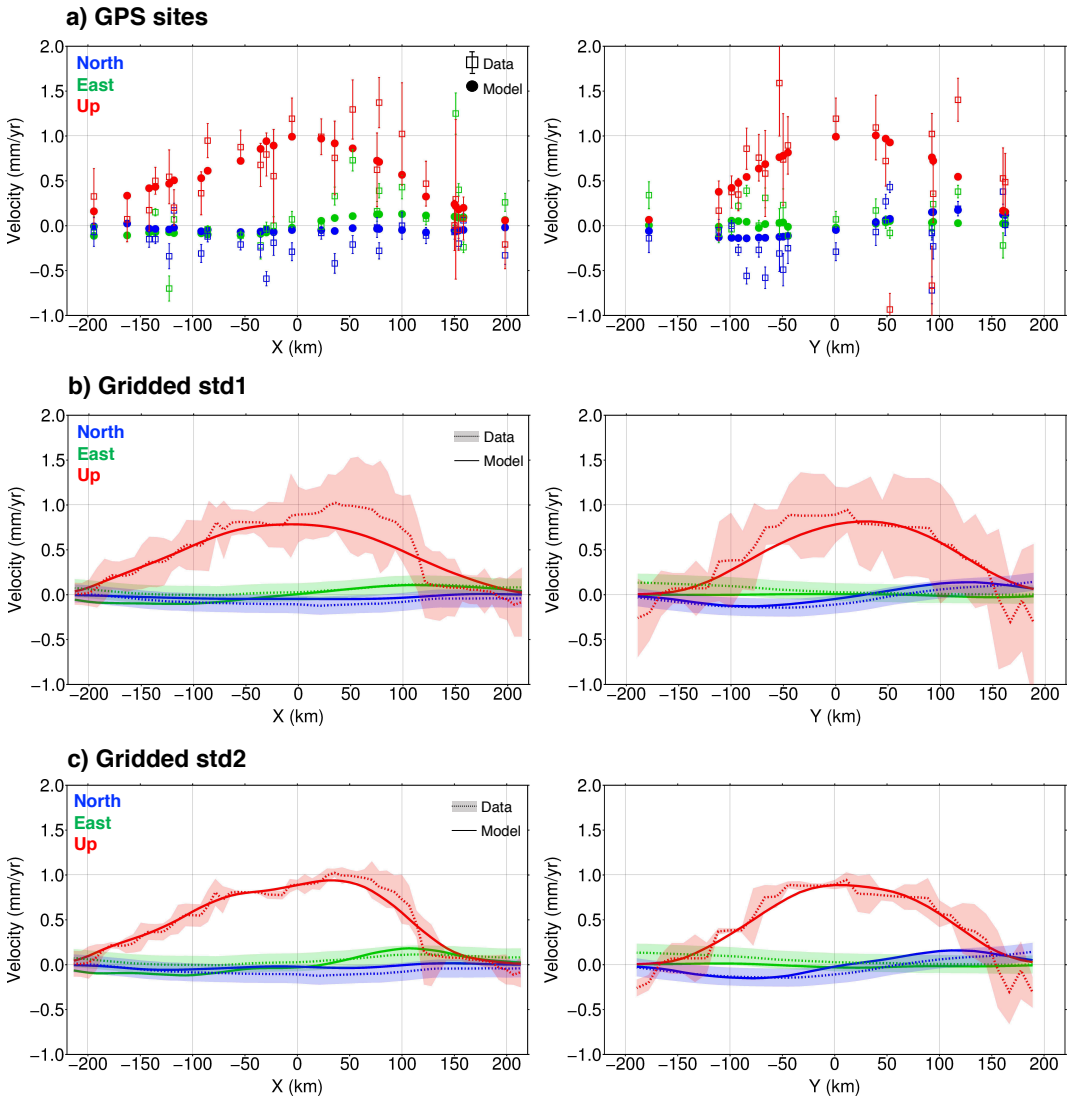

Figure S5. Comparison between data (and related uncertainty) and model results (TRDs grid at 30 km depth) along two profiles respectively along east-west (coordinate Y=0; left) and north-south (coordinate X=0; right).

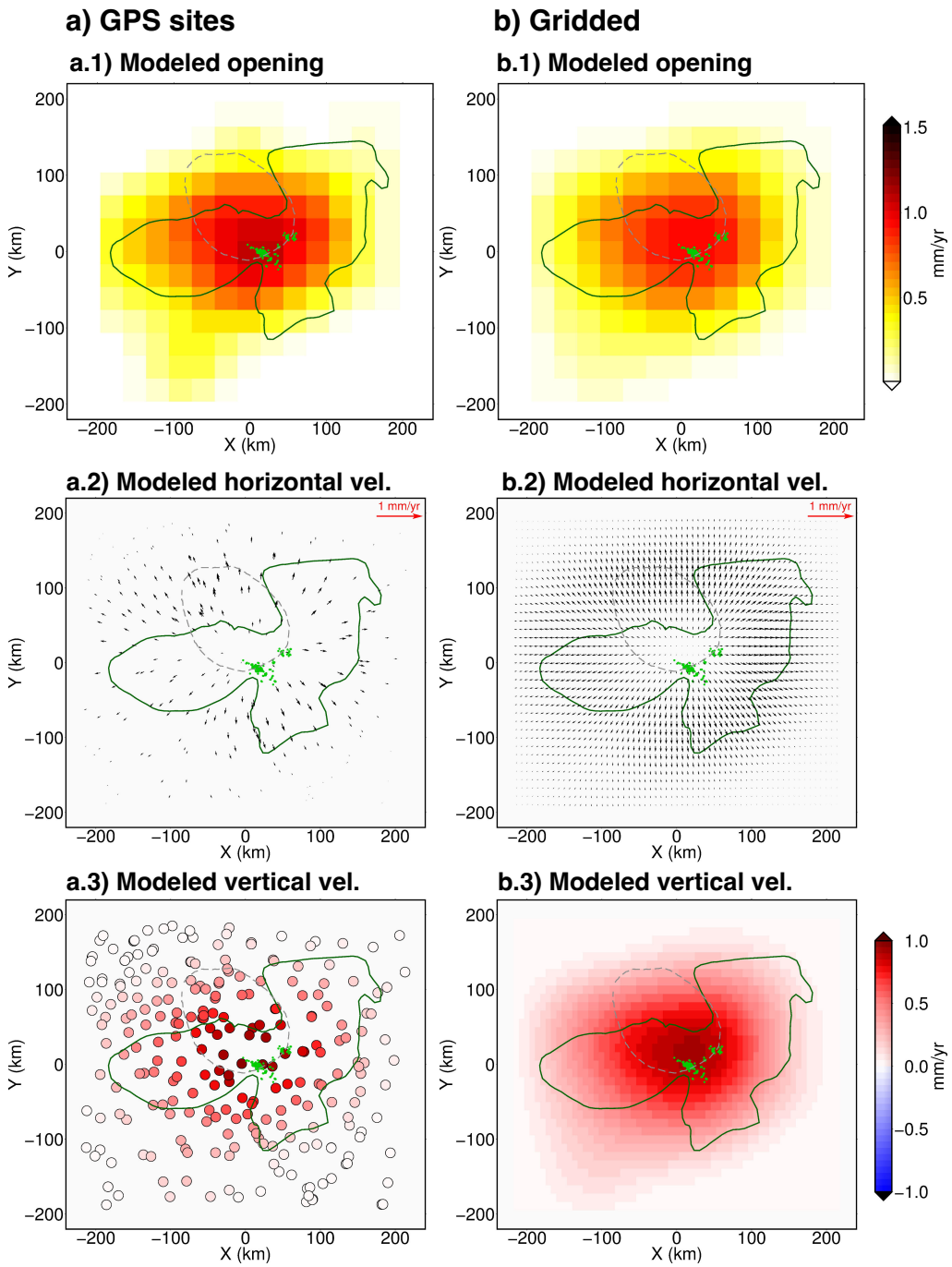

Figure S6. Model results for a TRDs grid at 30 km depth obtained using the different kinds of surface velocity data and equal weights ($\mathbf{W} = \mathbf{I}$). a) Results for GPS data (k=1e9 m*yr, RMSE = 0.53 mm/yr, volume rate = 4.65e7 m/yr). b) Results for gridded data (k=2e9 m*yr, RMSE = 0.1 mm/yr, volume rate = 4.38e7 m/yr). All other elements are the same as in Figure S1.

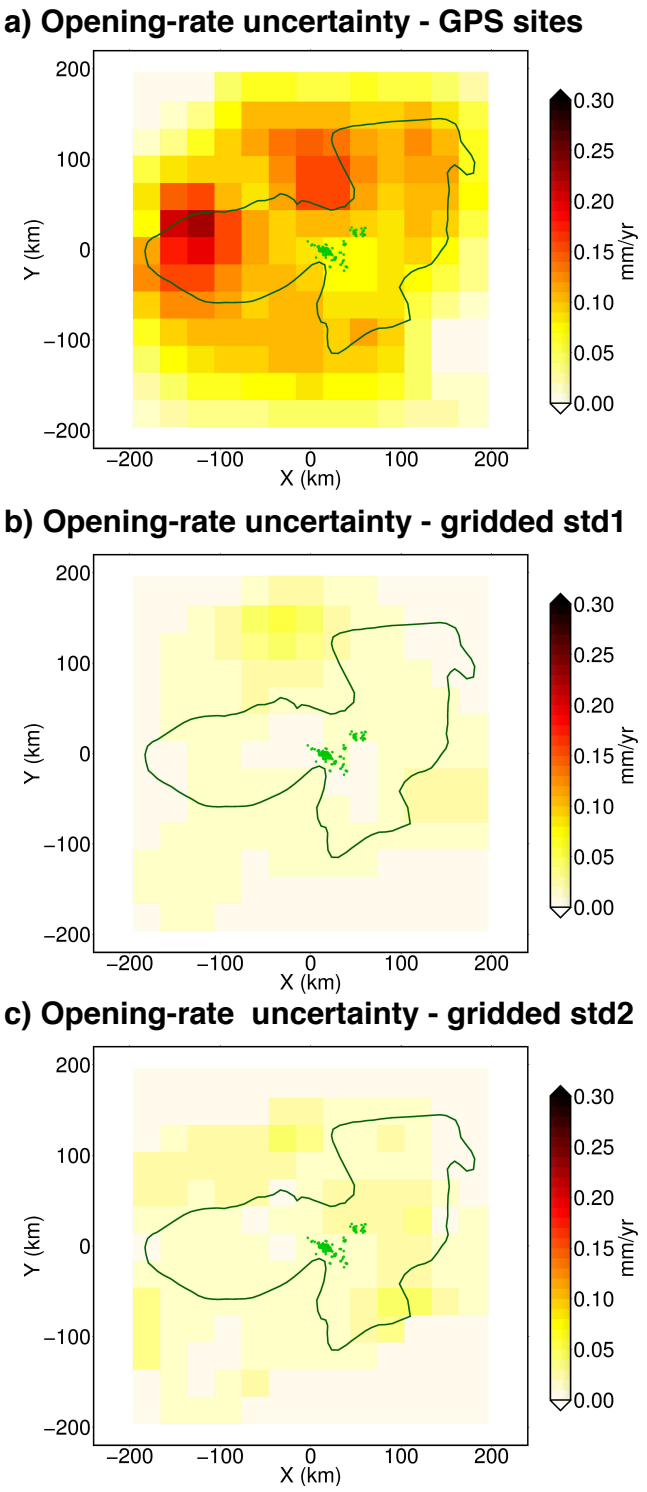

Figure S7. Opening-rate uncertainty distribution (1-σ standard deviation for each patch) for a TRDs grid at 30 km depth, obtained through bootstrap analysis and associated to the solution shown in Figure 2 of the main text. All other elements are the same as in Figure S1.

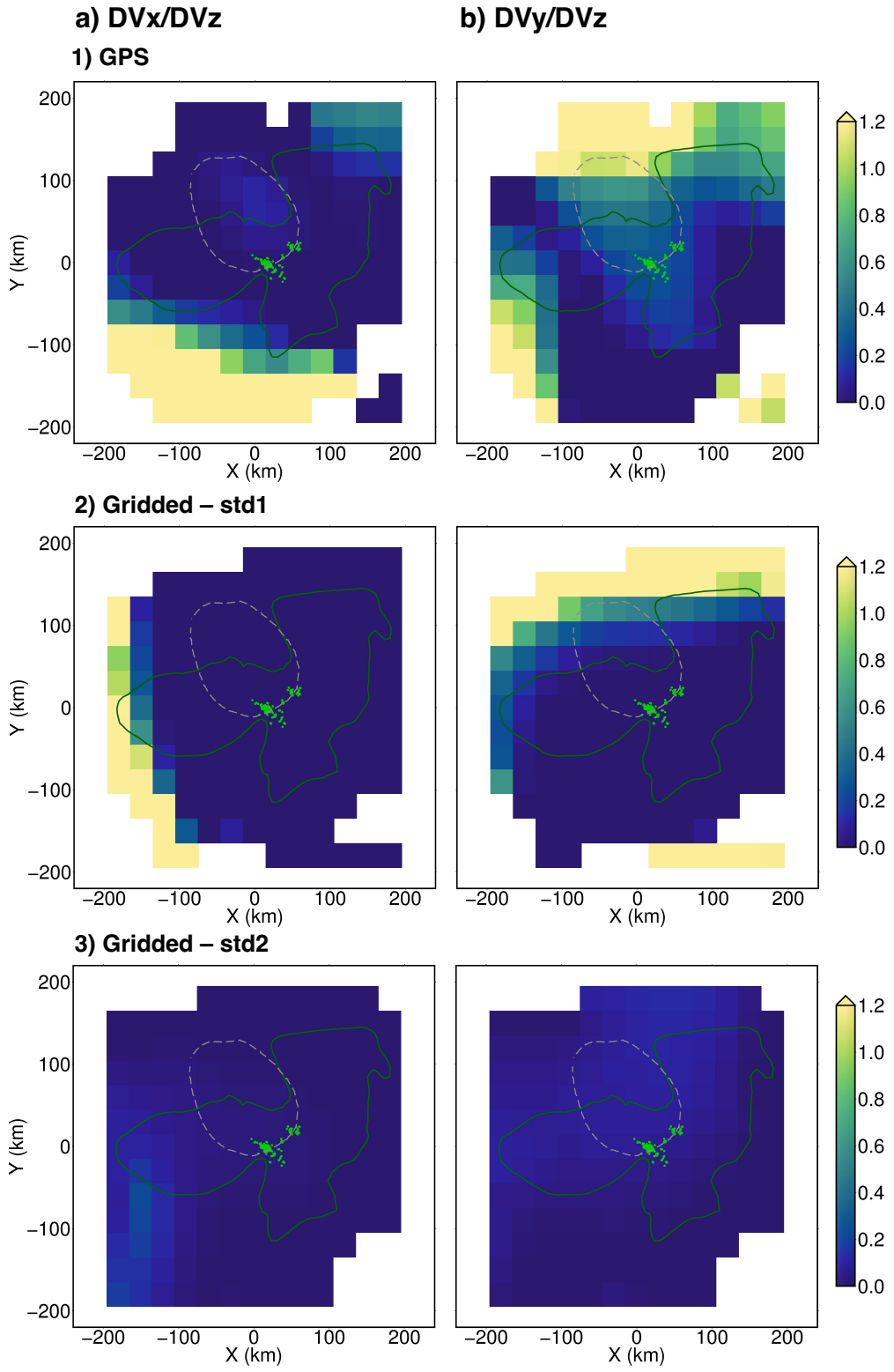

Figure S8. Spatial distribution of ratio between the horizontal (ΔV_x and ΔV_y) and vertical (ΔV_z) potency components of a grid of pCDMs at 30 km depth. Each raw correspond to results obtained using different kinds of data. All other elements are the same as in Figure S1.